Journal of Marine Research, 66, 751–773, 2008

Assessing the wind field over the continental shelf as a resource for electric power

by Richard W. Garvine[1,2] and Willett Kempton[1,3,4]

ABSTRACT

To assess the wind power resources of a large continental shelf area, we analyze the 18-year hourly wind records from meteorological stations in the US Middle Atlantic Bight (MAB), comparing areas of coast, estuary, and open shelf. We calculate winds at turbine hub height for the sea breeze compared with synoptic winds and, for each type of site, we compare the seasonal and daily phase match to electrical load. To improve large-scale ocean power resource calculations, we derive an iterative algorithm to determine the surface roughness coefficient (z_0). Our method calculates z_0 for specific times and locations over the ocean, rather than the prior practice of using a generic z_0 that is constant across time and space. Due to lower surface roughness of the ocean, wind speeds are notably higher at hub height, so that in the MAB we find that a representative open shelf site has three times the power content of a nearby land site. Regarding phase match to daily electric load, we find the sea breeze adjacent to the coast is a very good match to this region's electric power load profile. However, the open shelf wind speeds are so much higher (10.9 m s^{-1} versus 5.7 m s^{-1} for the comparison period) that the near-coast phase advantage is obviated. We also find more consistent wind power production offshore, with single sites producing at least some power 88 to 92% of the time. By modeling electrically interconnected sites, power production improves to 96.3% with as few as three interconnected wind sites and to 99.3% with 5 interconnected sites.

1. Introduction

A large resource of carbon-free electricity, close to populous coastal states, can be found in offshore wind power (Kempton *et al.,* 2007; Archer and Jacobson, 2003, 2005). Here we investigate the characteristics of that resource over the large continental shelf (approximately 1000 × 150 km) adjacent to the most urban stretch of the US East Coast, from Massachusetts through North Carolina. Four utility-scale (>300 MW) projects are in the planning and contracting stage in this region as we write, with electricity costs at parity with market price of new fossil generation (Delaware Public Service Commission, 2007; New Energy Opportunities, 2007). To locate, evaluate and plan development of this resource, there is a practical need to estimate the wind power resource over large ocean areas. Most meteorological station measurements are made at the 5 to 10 m

1. College of Marine and Earth Studies, University of Delaware, Newark, Delaware, 19716, U.S.A.
2. Deceased.
3. Center for Carbon-free Power Integration, University of Delaware, Newark, Delaware, 19716, U.S.A.
4. Corresponding author. ***email: willett@udel.edu***

height, but today's offshore wind turbine hubs are at 80 m to 100 m. The common practice is to extrapolate measured values to 80 m based on the log law, or law of the wall, which requires surface roughness as an input coefficient. Here we use this extrapolation as a basis for several measures of the wind resources, but additionally derive a method to estimate the surface roughness coefficient (z_0) based on conditions over the temperate sea.

We develop here methods for assessment that are general to most temperate oceans over continental shelves. These include the comparison of sites for average wind speed and power density, phase match to daily and seasonal load, constancy of wind in different types of sites, and increase in constancy by electrical interconnection of diverse sites. We then test these methods by analysis of one area, the Middle Atlantic Bight (referred to hereafter as the "MAB"). This region is particularly interesting for large-scale wind power, because it is adjacent to the electricity-hungry and carbon intensive urban corridor from Boston, MA, through New York City, to Norfolk, VA, and because these states' offshore wind resource is large enough to provide over four times their total electrical needs (Kempton *et al.,* 2007). Thus, we also develop measures of the match of wind to electrical load, and of output leveling by connecting diverse wind sites—methods needed to understand wind power if it should become a large fraction of electrical generation.

2. Model development

The total kinetic energy flux of a uniform air stream of speed U and density ρ passing through a turbine of area A is $P = \rho A U^3/2$ (Manwell *et al.,* 2002). To assess the basic size of the resource we employ the kinetic energy flux density $D = P/A = \rho U^3/2$ (W m^{-2}) which is entirely dependent on the air density and speed, not on the particular properties of a given wind turbine (Manwell *et al.,* 2002). We will refer to the kinetic energy flux density, D, as the "power density."

The wind regime for present and near future wind generators is the planetary boundary layer (referred to hereafter as "PBL"), which adjoins the lower troposphere. Typical PBL thicknesses are 1 km, while present wind generators' rotor hub height is only 80 to 100 m; therefore, a wind generator will experience the lower portion of the PBL most of the time. In order to estimate the size of the resource, some knowledge of the major physical characteristics of the PBL is necessary.

There are two essential differences between the PBL structure over land *vs.* water. First, the apparent surface roughness z_0 is much larger over land (Manwell *et al.,* 2002; Hess and Garratt, 2002), leading to higher wind speeds and thus more power generation over water. Second, most of the PBL over land is unstable, whereas most of the PBL over the temperate ocean of interest to wind power development (beyond nearshore and well above the surface) is mildly stable with downward heat flux to the ocean below (Webster and Lukas, 1992). A model that is restricted to nearly neutral conditions should be adequate for wind power analysis over most ocean areas, excluding tropical oceans with unstable conditions (and we shall calculate the effect of unstable conditions on our results). We assume modest variations in the PBL due to non-neutral conditions, variable wave age

(Moon *et al.,* 2004), and limited wind fetch. We ignore these here, in making our preliminary wind resource assessment, because they are secondary effects for the long-term, large-scale resources estimates we seek here.

The PBL model we used is a combination of Rossby similarity theory (Blackadar and Tennekes, 1968) and an independent relation between z_0 and the friction velocity u_*, valid for use over water (not land). This PBL model is by Charnock (1955), as generalized by Kraus and Businger (1994). In effect, the Kraus and Businger equation supplies z_0 to the Rossby model which has no constraint on z_0. Although the Rossby model has been used in the literature of dynamical meteorology, it has not often been used in the wind power literature. For example, one frequently cited source for z_0 over water (Barthelmie *et al.,* 1996) gives a fixed constant value of 0.002 m; however, this is entirely empirical, recommended because it was said to be "unlikely to lead to serious errors" (Barthelmie *et al.,* 1996). An unpublished estimate of US Atlantic wind resource used a constant value of 0.0002 m for the entire region, this value justified only because it was said to be recommended by another, experienced team (Berlinski and Connors, 2006, p 15). To provide a more theoretically grounded derivation of z_0, we have reduced the Rossby model and the Kraus and Businger model to a single governing equation, whose solution structure shows the branching structure of the system, including z_0. For a derivation of the equations and our method for computing, see Appendix A.

With model solutions in hand for z_0 and u_*, we invoke the log law or law of the wall (Charnock, 1955):

$$u(z) = \frac{u_*}{\kappa} \log\left(\frac{z}{z_0}\right). \tag{1}$$

Here κ is the von Karman constant, usually taken as 0.4.

The dynamical role of z_0 is best seen from its connection with the bottom drag coefficient C_d. By definition, $\tau = \rho u_*^2$ where τ is the surface wind stress. Relating this stress to the wind speed u_r at a reference height z_r, using the quadratic drag law $\tau = \rho C_d u_r^2$, and combining with the log law in (1) gives

$$C_d = \left[\frac{\kappa}{\log(z_r/z_0)}\right]^2 \tag{2}$$

Figure 1 shows the model results for C_d vs. the wind speed u_r at the reference height z_r, taken at 10 m here. Note the double-valued nature for C_d with an extremum (here a minimum) value at about 2 m s^{-1}. Values to the left of the minimum reflect "smooth" aerodynamic conditions when the roughness height z_0 is smaller than the molecular viscous boundary layer thickness ν/u_*.

Figure 2 shows the strong effect of z_0 (or C_d) on the wind profile within the log law region. Three profiles appear, one for the Rossby model (Hess and Garratt, 2002; Blackadar and Tennekes, 1968) and Charnock (1955) combined and the other two from the

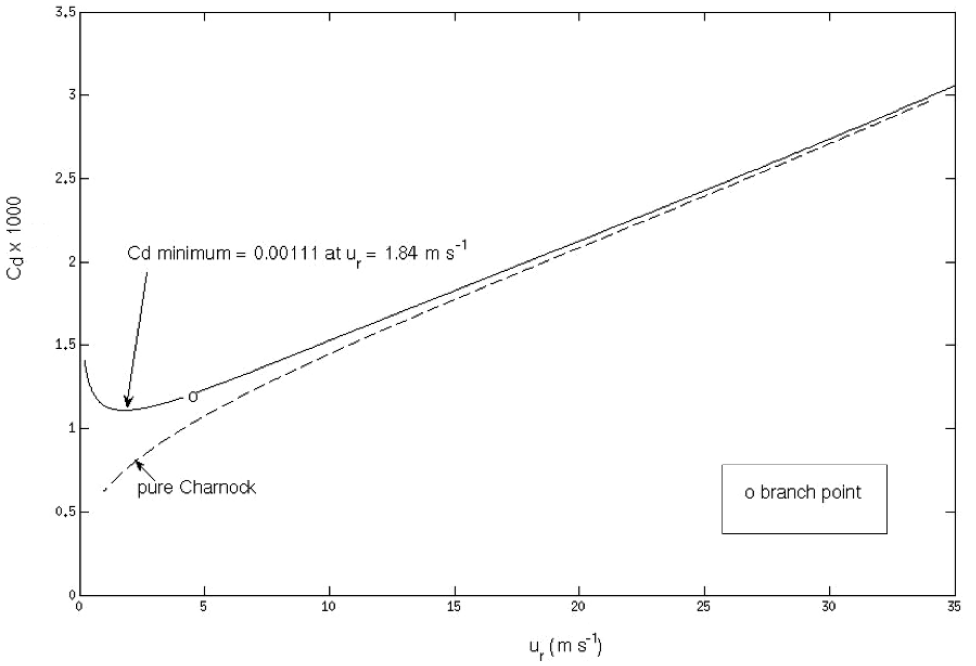

Figure 1. Surface drag coefficient C_d vs wind speed u_r at reference height (10 m) for the present model (solid curve). Dashed curve shows the same, but for the Charnock constraint only. The "o" marks the branch point, where the solution splits into smooth and rough branches.

former, but with imposed z_0. In Figure 2, the geostrophic wind above the PBL is fixed for all the profiles at $G = 10$ m s^{-1}.

The wind power density available to a wind turbine is given by $D = \rho U^3/2$ where U is the wind speed at hub height. For the three profiles shown in Figure 2, D varies at hub height from 180 to 369 W m^{-2}, or by a factor of about two over the full range. This strong tendency for wind speed to increase at a fixed level with decreasing C_d or z_0 explains much of the observed difference we will find subsequently when terrestrial sites are compared to ocean sites.

The impact of stable or unstable stratification within the log law region can be treated by using the model of Monin and Obukhov (Monin and Yaglom, 1966), which alters the log law formulation[5] of Eq. (1) to

$$u(z) = \frac{u_*}{\kappa}\left[\log\left(\frac{z}{z_0}\right) + 5\,\frac{z}{L}\right] \tag{3}$$

5. See, for example, the discussion by Turner (1973), pages 130–133. We adopt Turner's convention of positive L for stable conditions. This convention is preferred to make the sign of the momentum and the sign of heat flow both positive in the same direction.

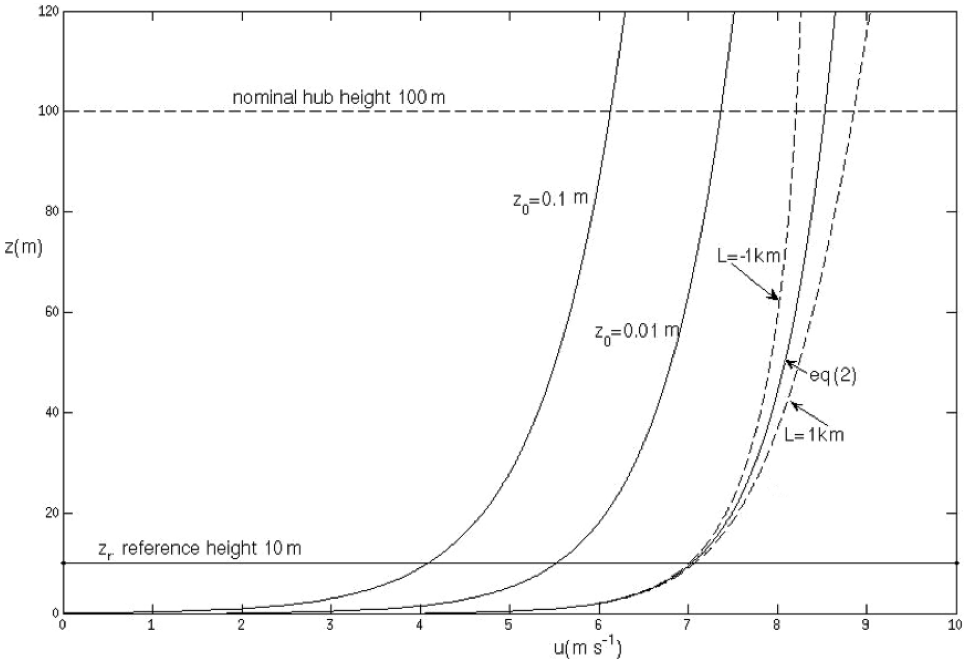

Figure 2. Wind speed profiles u versus height z for three cases, each with geostrophic wind above (approximately 1 km) at 10 m s^{-1}. The solid curve on right is for the present model which selects $z_0 = 0.000188$ m. The two dashed lines that bracket this solid curve are wind speeds for stable conditions ($L > 0$, right dashed curve) and unstable conditions ($L < 0$, left dashed curve), in this example with $|L| = 1$ km. The remaining two solid curves on the left are for the Rossby similarity model with user selection of z_0, as 0.1 and 0.01 m, typical of terrestrial sites.

where L is the Monin and Obukhov length given by

$$L = -\frac{u_*^3}{\kappa B_z}. \tag{4}$$

Here, B_z is the vertical buoyancy flux across the air-sea interface, positive upward, as when the water is heating the air above. For unstable stratification, $L < 0$, for neutral stratification, $B_z = 0$ and $L \to \infty$, and for stable stratification $L > 0$.

We illustrate the effect of stability and instability in the PBL on the wind profile from the model in Figure 2. At a given height, unstable stratification with $L = -1$ km and stable stratification with $L = +1$ km have a moderate impact on the wind profile with stronger winds for stable conditions and weaker winds for unstable conditions (e.g. Turner, 1973). The difference in wind speed at 100 m height is about 10%. In our assessment of the level of wind power available over the MAB, we expect mostly stable conditions. In our calculations, we assume neutral stratification and thus use Eq. (1), resulting in lower wind speed estimates than would be calculated from Eq. (3).

The distance vertically between typical weather buoy anemometer height (5 m) and hub height (80 m–100 m) usually occupies a substantial part of the log law region in the PBL. The ratio of the speeds at those two levels increases from about 1.2 at low speeds to about 1.5 at the highest speeds. More critically, the wind power density varies by a factor of about 2 to 3 across the same speed range.

Because of this steep vertical gradient of wind speed with height, we felt it necessary to check that the net power density spanning the large vertical range of a turbine disk is not significantly different from that obtained by the simplification of using only the point measurement of wind speed at hub height. The wind speed will be less over the lower half of the rotor disk and higher over the upper half. As shown by our derivation in Appendix B, this difference in power density is typically 1–2% and is at most about 4%. Thus, we shall subsequently neglect it in our analysis and use the simplification that the point wind speed at hub height is uniform over the disk.

3. Application to the wind field of the Middle Atlantic Bight

We examine wind data collected in the MAB. As shown in Figure 3, the MAB extends along the US East coast from Nantucket Island to Cape Hatteras, an 850 km span, or roughly 1,000 km of coast. On average, the shelf break is located about 100 km from the coast and the shelf bottom slope is about 0.001.

Our analysis compares wind on near-coastal lands, over the open shelf, and over an adjacent estuary. (By "open shelf," we mean that at the site there is unlimited fetch from at least 180° in continuous azimuth; for example, in Figure 3 site *ducn7* marginally satisfies this condition.) Table 1 gives measurement site locations and anemometer heights.

4. Wind speed at hub height

Substantial records of wind speed and direction were available from nine buoys moored on the open shelf (labeled "o" in Tables 1 through 4) and maintained by the NOAA National Data Buoy Center. The Center for Operational Oceanographic Products and Services of the NOAA National Ocean Service operated six other anemometers, two over the waters of the lower estuary (labeled "e"), and four along the estuary shoreline but at terrestrial sites (labeled "t"). We used wind records from one other site, Atlantic City, New Jersey ("ac") because it was at a terrestrial site yet near the coast. Record lengths ranged from 1.7 to 19.6 years with occasional short gaps that were filled by linear interpolation and by longer gaps that required the separation of the record into continuous pieces.

We now examine the wind resource in these two subregions (land versus ocean or estuary), including its time and space variations. A wind resource may be described with either the metric of "wind class," as velocity at a given height, or as power density. Traditionally, industry practice has been to categorize a site's wind resource into a class, defined by a range of mean speeds at a given height, $\bar{q}$. Following Elliott *et al.* (1987), classes 1 to 7 are defined, with class 1 defined as $\bar{q} < 5.9$ m s^{-1} (at 80 m height) and class 7

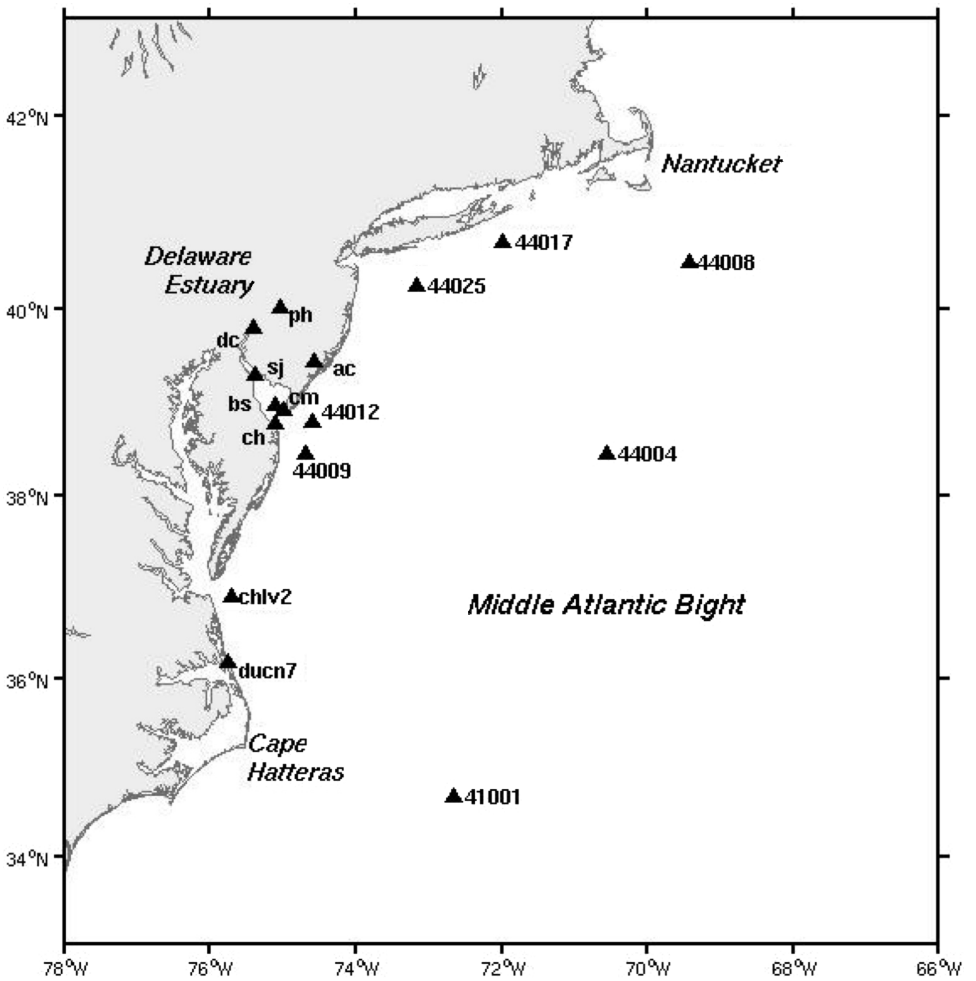

Figure 3. Location in the Middle Atlantic Bight and the Delaware estuary of the environmental buoys and terrestrial wind sites whose records were used in the present study. See Table 1.

for $\bar{q} > 9.4$ m s^{-1}. Because these classes are arbitrary and discontinuous, another metric used by the industry is simply $\bar{q}$, wind speed at a given hub height. Tables 2 through 4 give both wind speed at 80 m hub height and the corresponding wind class.

As we noted previously, the instantaneous power density available is proportional to the speed cubed (Manwell *et al.,* 2002). Denoting the bar symbol as the time average at a fixed point (Eulerian mean), the time averaged power density (neglecting variations in density) is

$$\bar{D} = \bar{\rho}\overline{q^3}/2. \tag{5}$$

The key property is then the time average of the speed cubed (not the cube of the mean speed $\bar{q}$). The power output from a real generator will, of course, always be less than the

Table 1. Wind data locations. Site ID is the met station designation, setting is "o" for open shelf, "e" estuary, or "t" terrestrial. Locations are shown in Figure 3.

Site ID	Setting	Latitude (deg. N)	Longitude (deg. W)	Anemometer height (m)
44009	o	38.46	74.70	5.0
41001	o	34.68	72.66	5.0
44001	o	38.70	73.60	5.0
44004	o	38.47	70.56	5.0
44006	o	36.30	75.40	5.0
44008	o	40.50	69.43	5.0
44017	o	40.70	72.00	5.0
44025	o	40.25	73.17	5.0
44012	o	38.80	74.60	13.8
chlv2	o	36.91	75.71	43.3
ducn7	o	36.18	75.75	20.4
bs	e	38.99	75.11	15.0
sj	e	39.31	75.38	15.0
ch	t	38.78	75.10	10.0
cm	t	38.93	74.98	10.0
dc	t	39.81	75.41	9.0
ph	t	40.01	75.04	9.0
ac	t	39.45	74.57	10.0

calculated power density of the resource, and generally the electrical output from a single device will not increase with the cube of wind velocity on that device.[6]

In the remainder of this section we show results for the wind speed variations in space and time that are relevant to assessment of the potential for wind generation offshore. The variable we use for this is the power density $\bar{D}$.

5. Wind speed variation by location and by season

The striking differences in wind speed among sites in Table 2 can be explained by their site location. All water sites (labeled "o" or "e") have power densities of 384–779 W m^{-2} and mean wind speeds at hub of 6.8 to 8.9 m s^{-1} (and class rankings of 3–5). By contrast, the terrestrial sites have substantially lower power density and wind speed. The marginal overlapping examples are terrestrial site *ch,* whose peninsular location gives it the highest

6. Real device power output is limited the Betz Limit (Manwell *et al.,* 2002) and by the usual mechanical and electrical losses of any real device. In addition, a wind generator's design is optimized for a given wind regime. Consequently, a wind generator is characterized by a power curve with zero electrical power output up to a minimal "cut in" wind velocity, followed by a narrow range of velocities yielding approximately the modeled cubic increase in power output, then inflecting, then flattening to maximum power at the "rated wind speed." Above this the power output is constant. Thus, in comparing sites, those with higher average velocities will typically yield more power, but not nearly as much as implied by the cubic function, Eq. (5).

Table 2. Record length properties from all wind observations at each site. Key: siteid and Setting are as in Table 1; meansp is the record mean speed at 80 m hub height (m s^{-1}); stdsp is the speed standard deviation (m s^{-1}); erspd is the standard error of the speed (m s^{-1}); $\bar{D}$ is the power density mean (W m^{-2}); length is record length (years); class is wind class; %act is "percent active" calculated by counting hours for which speed >3 (m s^{-1}); % Weibull is the percent active as estimated from the Weibull fit.

siteid	Setting	meansp	stdsp	erspd	$\bar{D}$	stdE	errE	Length	Class	%act	%Weibull
44009	o	7.93	4.12	0.14	569	882	16	17.9	4	90	90
41001	o	8.68	4.16	0.16	684	952	18	15.9	6	92	94
44004	o	8.93	4.48	0.19	779	1125	24	12.5	6	93	92
44008	o	8.22	4.49	0.15	673	1120	21	16.8	5	89	89
44017	o	8.73	4.42	0.44	732	1019	51	2.3	6	92	92
44025	o	8.15	4.10	0.17	598	878	18	13.3	5	92	91
44012	o	7.40	3.95	0.22	475	758	23	6.3	4	88	87
chlv2	o	7.74	3.91	0.13	512	787	13	19.6	4	89	90
ducn7	o	6.95	3.52	0.18	384	748	20	8.1	3	90	88
bs	e	7.70	3.88	0.41	514	1021	54	2.0	4	91	90
sj	e	6.83	3.58	0.38	384	1121	62	1.9	3	88	86
ch	t	5.74	3.88	0.30	309	632	33	2.1	1	74	74
cm	t	4.90	3.00	0.28	172	390	23	1.7	1	72	71
dc	t	3.75	2.40	0.19	81	195	10	2.1	1	55	57
ph	t	2.63	1.57	0.13	26	56	3	2.2	1	33	36
ac	t	4.99	2.60	0.09	146	263	5	18.3	1	76	76

wind speed of the terrestrial sites and marginally higher power density than the least energetic water site, *sj,* an upper estuary site bracketed by land.

Figure 4 is a summary map of the wind resource, drawn from Tables 3 and 4. At each site circles are drawn with centers on the buoy sites and with areas proportional to $\bar{D}$ averaged over three winter months (larger circles) and over three summer months (smaller circles). The winter and summer months can be distinguished by size alone because at every measurement site on this map, $\bar{D}$ is larger in winter. There is surprisingly little horizontal difference in $\bar{D}$ over the ocean for a given season. That is, the open shelf sites in this area have a large and spatially uniform power density. Winter averages are about 4:1 greater than those of summer. For today's electricity market, higher winter and lower summer power density is a disadvantage for wind power over, say, solar power, in that wind power's annual variation is out of phase with market demand in this region. This is because of the currently high proportion of electrical power used for air conditioning versus fossil fuels for heating. However, if this area has expensive fuels and inexpensive electricity over several decades, that will presumably shift equipment choice in the building stock.

Terrestrial location of a site results in lower wind speed and thus much lower power density $\bar{D}$. For example, comparing the year long average of Atlantic City (*ac*) with buoy 44009 in Table 2, we find 146 vs. 569 W m^{-2}. One need not travel very far from dry land to locate a windy site. Even the site at *bs* in the lower Delaware estuary is much more

Table 3. Winter wind statistics. Column labels are as in Table 2.

siteid	Setting	meansp	stdsp	erspd	$\bar{D}$	stdE	errE	Length	Class	%act
44009	o	9.48	4.59	0.36	893	1175	44	4.0	7	93
41001	o	10.61	4.59	0.42	1128	1271	51	3.6	7	95
44004	o	10.98	4.81	0.46	1262	1451	60	3.3	7	96
44008	o	10.67	4.96	0.41	1225	1544	60	3.8	7	95
44017	o	11.34	4.34	1.13	1262	1251	124	0.6	7	98
44025	o	10.11	4.50	0.43	999	1164	49	3.2	7	95
44012	o	8.75	4.32	0.54	715	971	60	1.5	6	92
chlv2	o	8.69	4.14	0.30	677	887	30	4.9	6	91
ducn7	o	7.45	3.73	0.41	459	734	40	1.9	4	91
bs	e	9.03	4.08	0.97	738	1257	135	0.5	7	95
sj	e	7.79	4.02	0.85	569	1858	203	0.5	4	91
ch	t	7.46	4.39	0.80	535	795	86	0.5	4	84
cm	t	5.88	3.42	0.73	265	452	56	0.4	2	79
dc	t	4.30	2.57	0.44	109	241	24	0.6	1	65
ph	t	3.00	1.64	0.30	34	59	6	0.6	1	43
ac	t	5.46	2.91	0.19	195	336	12	4.5	1	81

energetic than that at *ac,* 514 vs. 146 W m^{-2}. An open shelf site is not critical, but an aquatic vs. terrestrial one is. As Barthelmie and Palutikof (1996) showed, the wind power density builds rapidly in the PBL as one changes sites by crossing the coast headed seaward. In our example from the MAB, this is true whether in the Delaware estuary or on the open continental shelf. The strong change in roughness height z_0 or in bottom drag C_d

Table 4. Summer wind statistics. Column labels are as in Table 2.

siteid	Type	meansp	stdsp	erspd	$\bar{D}$	stdE	errE	Length	Class	%act
44009	o	6.37	3.13	0.22	280	471	16	4.7	2	86
41001	o	7.06	3.19	0.26	349	510	19	4.3	3	89
44004	o	6.83	3.31	0.30	341	544	24	3.0	2	88
44008	o	5.91	2.95	0.21	228	388	14	4.6	2	83
44017	o	6.16	2.75	0.71	229	290	33	0.4	2	87
44025	o	6.41	2.95	0.26	268	394	16	3.4	2	89
44012	o	5.83	2.94	0.36	221	428	26	1.5	1	84
chlv2	o	6.36	3.18	0.22	283	543	19	4.8	2	85
ducn7	o	6.13	2.90	0.32	248	548	28	2.2	2	88
bs	e	6.19	2.82	0.64	248	857	89	0.5	2	89
sj	e	5.82	2.79	0.68	215	605	70	0.4	1	87
ch	t	4.10	2.42	0.39	96	219	21	0.6	1	64
cm	t	3.93	1.94	0.41	66	101	10	0.5	1	66
dc	t	2.98	1.70	0.33	35	75	8	0.5	1	43
ph	t	2.03	1.09	0.22	10	22	2	0.5	1	18
ac	t	4.28	1.93	0.15	79	114	4	4.7	1	7

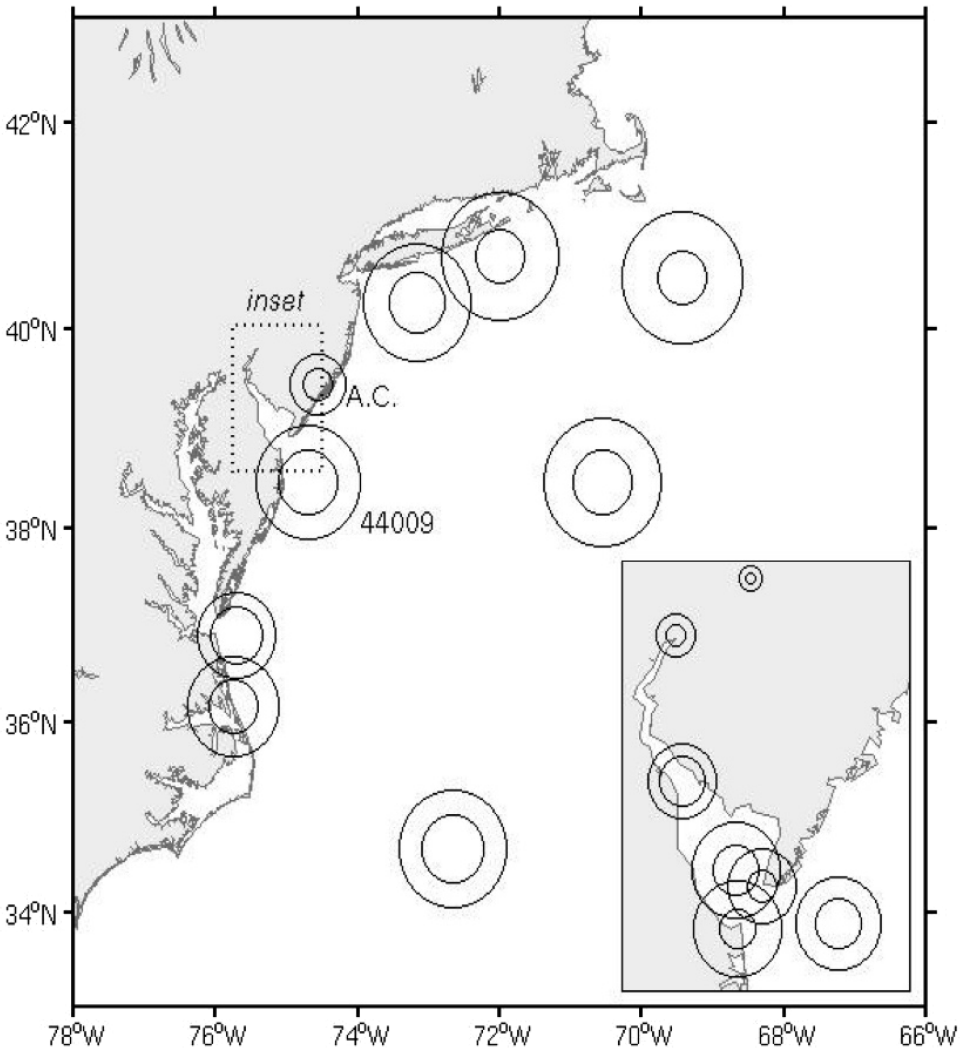

Figure 4. Available power density from the wind for the three winter months (larger circles) and the three summer months (inner circles) for each measurement site. The inset at the lower right shows the Delaware estuary sites. The area of each circle is proportional to the power available; the scale of the circles in the inset map is equal to that on the larger map, not proportional to map scale.

noted in section 2 explains the striking difference well—given the same geostrophic wind G aloft, the wind profile $u(z)$ has much greater speed near the surface for lower z_0 (See Fig. 2).

6. Phase match of wind speed to daily electrical load

How is the wind field over the MAB distributed over time of day? We have already indicated how the wind kinetic energy varies seasonally, but variations of wind speed with

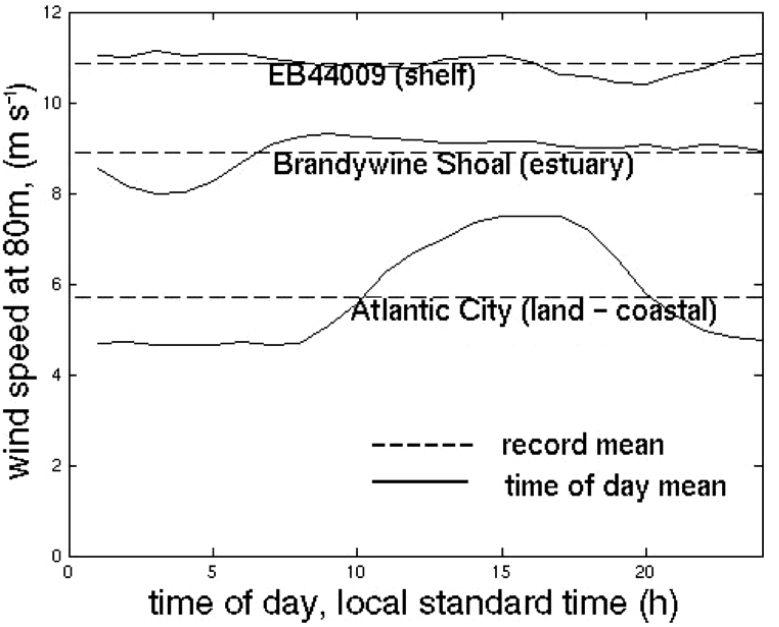

Figure 5. Time of day average wind speed at 80 m height for three sites: buoy 44009 in the open shelf, Brandywine Shoal in Delaware Bay, and Atlantic City, NJ on land adjacent to the coast.

time of day are also relevant to electric power generation and load matching. We used simultaneous wind records from: EB44009, a buoy about 40 km off the Delaware coast, a weather station at *ac* (Atlantic City airport), and another buoy at one of the estuarine sites (*bs*). These three compare an open water site on the shelf with both a terrestrial (albeit coastal) site and an estuarine site. We sorted the hourly data into 24 hourly bins, selected only those hours for which all three stations had data, a total of two years, then averaged each site's wind speed within each hourly bin. The results appear in Figure 5. The daily mean wind speed at the terrestrial site, *ac,* was 5.7 m s^{-1}, quite a bit lower than the other two, as we have already seen. At 44009 the speed was about 10.9 m s^{-1}, and at *bs* it was 8.7 m s^{-1}.[7]

The open shelf 44009 has much less diurnal variability, an amplitude of only 0.25 m s^{-1}. At *bs,* diurnal variability was comparably small compared to its mean value. The corresponding amplitude for terrestrial *ac* is 1.4 m s^{-1}, a variability of 25% of the mean. The phase of the *ac* wind in Figure 5 shows maximum speeds in the afternoon hours and minimums at night. This is clearly due to the sea breeze circulation, driven by the differing thermal properties of water and earth and consequent diurnal swings in temperature

7. These mean values in Figure 5 are a bit higher than those in Tables 2 and 3 because they were drawn from only two years' data, the time of data available from all sites. Those two years' means happened to be more energetic than those in Table 2, drawn from each measurement site's entire record, i.e. as many as 18 years.

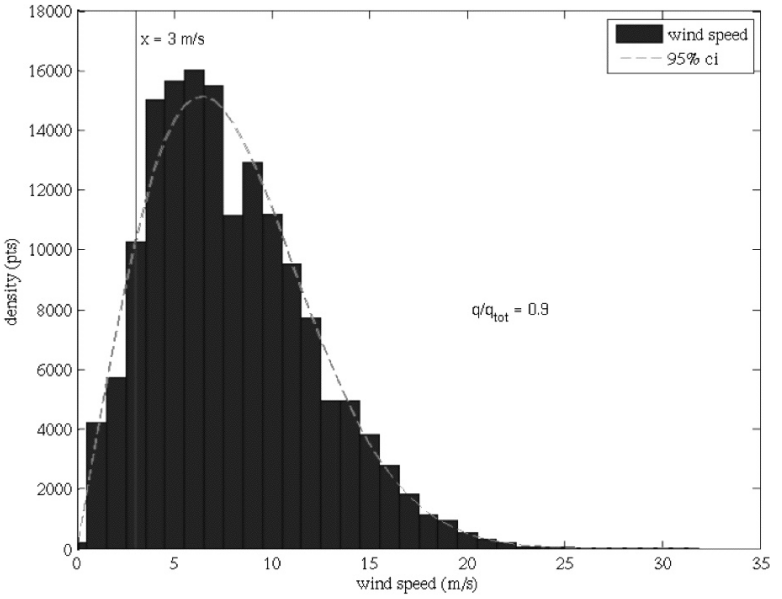

Figure 6. Probability density function (pdf) for wind speed at buoy 44009 (bar graph) and the best fit for the Weibull pdf (dashed curve). The record used is from January 1984 to December 2004. The cutoff speed for practical wind power generation is shown at 3 m s^{-1}.

differential. Because peak summer electrical loads are higher in the afternoon (Schlabbach and Rofalski, 2008), some have suggested the sea breeze as a good phase match to the diurnal swing of electrical load. (If we examine summer only, the sea breeze is more pronounced and thus the match of wind resource to summer afternoon electrical load is even better.) However, if the magnitude of the differences we observe in Figure 5 is typical of the sea breeze regime in other locations, the phase advantage of sea breeze is dwarfed by the far larger wind speeds over the open shelf waters. We expect synoptic winds to be much stronger than the sea breeze in most locations, as seen here. Although the present analysis makes the open shelf sites seem much more attractive, other considerations—such as lower cost for turbine installation and maintenance at terrestrial sites, or need for high electric generation reliability during load peak, or a local sea breeze intensified by topographic features such as the convergent channels common on the U.S. west coast—may favor sites with sea breeze.

7. Probability density function

The probability density function (pdf) of the wind speed also provides insight. In Figure 6 the pdf from the observed speed distribution at 44009 is indicated by the bars, in increments of 1 m s^{-1}. For comparison, the best-fit Weibull (Manwell *et al.,* 2002) pdf is shown as the smooth dashed line. The analytic form for the Weibull pdf y is

$$y = \frac{k}{c}(u/c)^{k-1}e^{-(U/c)^k} \tag{6}$$

where u is the wind speed and the two parameters of the distribution are c and k, determined by least square fitting.

In present technology for wind turbine generators, practical wind power extraction requires that the instantaneous wind speed exceeds a cutoff value of approximately $x_c = 3\ \mathrm{m\ s^{-1}}$. The Weibull probability density function (pdf) will enable us to make an estimate of the fraction F_c of the total wind energy that cannot be extracted by the generator (Manwell *et al.,* 2002).

$$F_c = \int_0^{u_c} y\,du = 1 - e^{-(u/c)^k}. \tag{7}$$

From Figure 6 for 44009, $F_c = 0.1$. That is, the extraction of power at 44009 is predicted to be operative 90% of the time. This equals the fraction previously computed for this site from hourly observations, as shown in Table 2 in the column labeled "percent active." The rightmost two columns of Table 2 list the counted hours and Weibull-predicted percent active, showing the close correspondence, most within 1%. The Weibull distribution pdf thus seems useful for the MAB data we analyze here, allowing computations of several characteristics from the pdf without recourse to repetitive computation from hourly data. The utility of the Weibull distribution has previously been accepted for most terrestrial wind sites based on prior analysis.

8. Persistence of generation from multiple interconnected sites

As Table 2 indicates, the persistence of wind speeds exceeding $3\ \mathrm{m\ s^{-1}}$ offshore is substantial. Annual mean percent active values range from 88 to 92% for all the offshore and lower estuary sites, while for the five terrestrial sites, they range from 33–76%. Thus, the common viewpoint that wind power is intermittent may be more applicable to terrestrial wind generators than to oceanic ones. Rather than calling these water sites "intermittent," a better description would be that they produce varying output (in contrast to a fuel-driven power plant, whose output is controlled by the operator).

Modern electric power grids interconnect many generators to increase reliability when conventional plants fail. Thus to reduce the variance of offshore wind power, one might combine power from different sites. Accordingly, we searched the wind records for those times when multiple sites were inoperative simultaneously (here we use $q < 3\ \mathrm{m\ s^{-1}}$). Direct computations from the year-long records of the nine offshore sites gave the fractional time when any two sites were both not producing at 10.6%, for three sites 3.7%, for four sites, 2.1%, and for five sites, 0.07%. During the year investigated, there was never an hour that fewer than three of these nine sites would have been producing power (at least $3\ \mathrm{m\ s^{-1}}$ wind).

That is, by connecting all nine sites during this sampled year, at least five would be producing power all but 0.7% of the time, and at least three would be producing all the time. That is, considering the interconnected sites as a single generator, it would never shut down. This is substantially better than the 6% forced outage rate for fossil generators (North American Electric Reliability Council, 2005). However, our "downtime" is only a preliminary measure; a more complete analysis is needed of partial-capacity generation (Archer and Jacobson, 2007; Kempton *et al.,* 2007) and its match to fluctuating load as opposed to just fractional downtime. Wind would not appear so invariant with this more complete comparison. As a countervailing factor, we expect the greatest variation in ocean weather to be at the synoptic weather scale, about 1,000 km horizontal scale. A preliminary analysis of the region we examined has been conducted, but since the MAB is only 850 km in longest extent, we would expect greater inter-site variation (and thus more steady combined power output) if a larger region, such as the 2500 km US Eastern Seaboard, were examined. These are areas for further investigation.

9. Concluding remarks

We have analyzed meteorological records in the MAB of the U.S. east coast to make a preliminary assessment of the wind energy resource size and power generation-relevant characteristics. This region is of particular importance because it is collocated with large electric power demand from the adjacent populated coastal cities. We used a standard model for the PBL that combined Rossby similarity with the Charnock relation as generalized by Kraus and Businger (Appendix A). This yielded a rational way by which to estimate the roughness parameter z_0 as opposed to the prior practice of selection of an arbitrary z_0. Our method is valid for analyzing wind over most non-tropical ocean regions, because the PBL stratification is generally mildly positive (stable).

After computing the bulk PBL properties, we invoked the log law or law of the wall to extrapolate the wind velocity vertically from typical anemometer heights of 5 to 10 m to hub heights of at least 80 m expected for offshore wind turbines.

Multi-year hourly wind data from nine buoys on the open continental shelf and two in an estuary were examined and compared with data from five nearby terrestrial sites. The empirical study showed higher wind speeds and much higher available power over water. In accordance with the findings of other investigators, the difference in roughness height z_0 or in surface drag coefficient C_d explain the striking wind speed difference, even with the same geostrophic wind G aloft. Consistently with most terrestrial wind studies, we find that the observed pdf for ocean sites is close to the Weibull pdf.

Annual and daily variations were also examined for phase match with electrical loads. Annual variation is not well matched to today's US electrical loads, which are higher in the summer due to predominance of electrical air conditioning versus predominance of fossil fuels for heating. The annual wind pattern would be better suited to countries with more electrical heating; US heating may evolve in this direction if fuels become more expensive and winter electricity abundant. Regarding time-of-day phase match, there is little

time-of-day power variability over the ocean whereas coastal terrestrial sites typically have a peak power output in the late afternoon due to the sea breeze. However, this excellent time-of-day phase match of coastal wind to load is overwhelmed by the much larger mean power available offshore and in the open part of the estuary.

To understand consistency of electrical output, we examined the persistence of wind speeds exceeding 3 m s^{-1} because that is the cut-in speed of present wind power generators. Annual mean percent active (speed $>$ 3 m s^{-1}) values range from 88 to 92% for all the offshore and estuary sites, while the five terrestrial sites are active only 33 to 76% (Table 2). To reduce the intermittency of wind power generation, one strategy is to electrically combine power from multiple sites. Combining year-long records from the nine offshore sites in various combinations, we find with two sites the fractional time of no power was 10%; for five sites, it was 0.07%. Considering all nine sites, there was never an hour in the year of zero power, in fact, there was never an hour for which fewer than three of the nine turbine sites would be producing power. Given that one concern about wind power is its intermittency, a more thorough study of multi-site ocean wind invariance is called for. A more thorough analysis should examine varying output levels and extend to sites separated by more than 1,000 km.

The size, strength, and steadiness of the potential wind generating resource we find for the MAB motivates a more detailed survey of the resource along all US coasts, as well as all continental shelves near population centers worldwide. We do not estimate the total MAB power generation resource here; however, a preliminary estimate (Kempton *et al.,* 2007) suggests that it is over four times the total present electrical needs of the adjacent coastal states. The large resource size, along with our analysis of wind speed and invariance, the rapid growth of the commercial wind industry, and the competitive electricity price for the first utility-scale offshore wind developments (Delaware Public Service Commission, 2007), suggest that offshore wind is a near-term option for significant carbon reductions by coastal states.

Acknowledgments. We give special thanks to Michelle Overway and John T. Reager for their processing of the data, analysis, and graphics, and to Fabrice Veron and Mimi Gerstell for detailed suggestions on ocean-atmospheric dynamics. Jane Branden edited the manuscript and improved the writing. Suggestions by several careful journal reviewers have improved the analysis and references. We express our gratitude to the College of Marine and Earth Studies at the University of Delaware for support of the project. The second author (Kempton) expresses his deep appreciation for having had the opportunity to work with the first author, Richard W. Garvine, now deceased.

APPENDIX A

A compact model of the neutral planetary boundary layer for ocean application

We draw from Rossby similarity theory for the PBL (Manwell *et al.,* 2002; Hess and Garratt, 2002) with Charnock's (1955) constraint, developed from measurements over water, connecting z_0 with the friction velocity u_* to close the mathematical problem. Here we reduce this system of equations to a single equation in a dimensionless variable that

clearly reveals the inherent branching structure of the solutions—one branch for aerodynamically rough conditions, the other for smooth conditions. The emphasis here is on simplicity and use of well tested components, so we omit the more subtle and less firmly established effects that are the subjects of contemporary research, such as wave age and finite fetch for the wind over the water.

The x-axis of the model is aligned with the wind and surface stress, which is inclined at the across-isobar angle α to the geostrophic wind aloft. The z axis is measured vertically from the sea surface upward.

Using the two horizontal momentum equations and applying asymptotic analysis, the Rossby model gives two independent transcendental algebraic equations which when written in dimensionless variables, are

$$\log q = A - \log Ro + B\sqrt{\left(\frac{\kappa}{qB}\right)^2 - 1}. \tag{A1a}$$

$$\alpha = S \sin^{-1}(qB/\kappa). \tag{A1b}$$

Here $q = u_*/G$ with $u_* \equiv \sqrt{\tau_b/\rho}$ the friction velocity, τ_b is the surface stress, and $S = f/|f|$, with f the Coriolis parameter. S is used to select the proper hemisphere. G is the speed of the geostrophic wind above the PBL, $Ro \equiv G/(|f|z_0)$, the Rossby number, κ is the von Karman constant $=0.4$, and A and B empirical constants equal 1.4 and 4.7, respectively (Kraus and Businger, 1994). Angle α is the across-isobar angle, that is, the angle between the direction of the geostrophic wind just above the PBL and the direction of the surface stress τ_b at $z = 0$.

To gain the most concise form for the model, we use dimensionless variables. To solve the system given by (A1), we take the independent variable to be Ro, typically 10^8 to 10^9, and solve (A1a) for the dependent dimensionless variable q by iteration, then find α from (A1b). The variation of q with log Ro is nearly linear and is very close to the log-linear variation found by Kraus and Businger (1994). The variation of α with Ro is also nearly log-linear with values that range from about 23° to 17°. Hess and Garratt (2002) compared these results for q and α with observations made over water and found good agreement.

We still lack values for z_0 and u_*. Eq. (A2) gives in dimensional variables the Charnock constraint together with the two terms added by Kraus and Businger. For z_0 as a function of u_*,

$$z_0 = C_1(u_*^2/g) + C_2(\nu/u_*) + C_3\sqrt{\nu u_*/g}. \tag{A2}$$

Here ν is the kinematic molecular viscosity, g is the acceleration of gravity, and the three dimensionless coefficients C_1 to C_3 are determined from laboratory or field data. The first term on the right is the original Charnock (1955) constraint, the second term introduces the viscous boundary layer thickness ν/u_*, and the third accomplishes a smooth transition between the first two terms.

The preferred choices are $C_1 = 0.0185$ (Wu, 1980), $C_2 = 0.11$, and $C_3 = 0.088$

(Kraus and Businger, 1994). Eq. (A2) can be recast in terms of dimensionless parameters and variables. We multiply each term by u_*/ν and introduce the roughness Reynolds number $Re \equiv u_* z_0/\nu$, a measure of the roughness height to the laminar boundary layer thickness very near the surface. Introducing the dimensionless dependent variable $Q \equiv \sqrt{u_*/(\nu g)^{1/3}}$ and using the definition of Re in (2) yields

$$Re = C_1 Q^6 + C_2 + C_3 Q^3. \tag{A3}$$

A second relation for Re is found by equating the roughness height z_0 in the definitions of and Ro to give $Re = Q^4/(qFRo)$ with $F \equiv |f|(\nu/g^2)^{1/3}$ a dimensionless measure of earth rotation, the *single* dimensionless parameter of the system. Equating the latter expression for Re with the former in (A3) yields the dimensionless governing equation for the system, a sixth order algebraic equation in Q:

$$C_1 Q^6 - (qFRo)^{-1} Q^4 + C_3 Q^3 + C_2 = 0. \tag{A4}$$

Recall that C_1, C_2, and C_3 are fixed constants, while q is a function of Ro that is already known. Hence, (A4) will give us $Q(Ro)$; then we get $Re(Ro)$ from (A3).

In general, Eq. (A4) has six roots following the degree of the algebraic equation. Two of these, numbers 4 and 5, are always complex conjugates and therefore correspond to no physical solution of (A4). The other four roots present possibilities for solutions. A representative case for the real part of Q is plotted in Figure A1 for the parameter $F = 5.4 \times 10^{-7}$ corresponding, for example, to $f = 1 \times 10^{-4}$ s^{-1}, $\nu = 1.5 \times 10^{-5}$ m^2 s^{-1} and $g = 9.81$ m s^{-2}. Root 1 has a value of about 6 at $Ro = 10^8$, then falls to about 4 with increasing Ro where it switches signs with root 2, which has been its mirror image about the Ro axis until then. For still larger Ro, root 2 reaches a branch point that corresponds to that in Eq. (A2). Here it joins smoothly with root 3, which has lower values of Q. To the right of this branch point, roots 2 and 3 become complex conjugates and are no longer of physical relevance. Meanwhile, root 6 is low in magnitude, negative, and nearly invariant with Ro, and is therefore rejected.

There are several possibilities for a physically relevant solution based on the solutions for Q. How do we choose the correct root or roots? Our criteria for a physical solution are that (1) the selected branch or branches be continuous in Ro and (2) the full range of physically plausible values be covered. We meet these criteria uniquely by starting with root 1 at low Ro and continuing until we reach its swap point with by root 2, then root 2 until the branch point with root 3, then root 3 back to low Ro.

Having selected these roots, we then find the variation of Re with Ro as shown in Figure A2. The part of the curve below the branch point is the "smooth" branch, so named because it represents the behavior for nearly aerodynamically smooth surface flow, as the small values of Re make clear. In contrast, the values for the other branch above the branch point have $Re > 1$, and so that branch is termed the "rough" branch.

For a smooth wall, the state of the shear flow there is laminar, viscous with boundary layer thickness ν/u_*; consequently, Re is just the ratio of the surface roughness height to

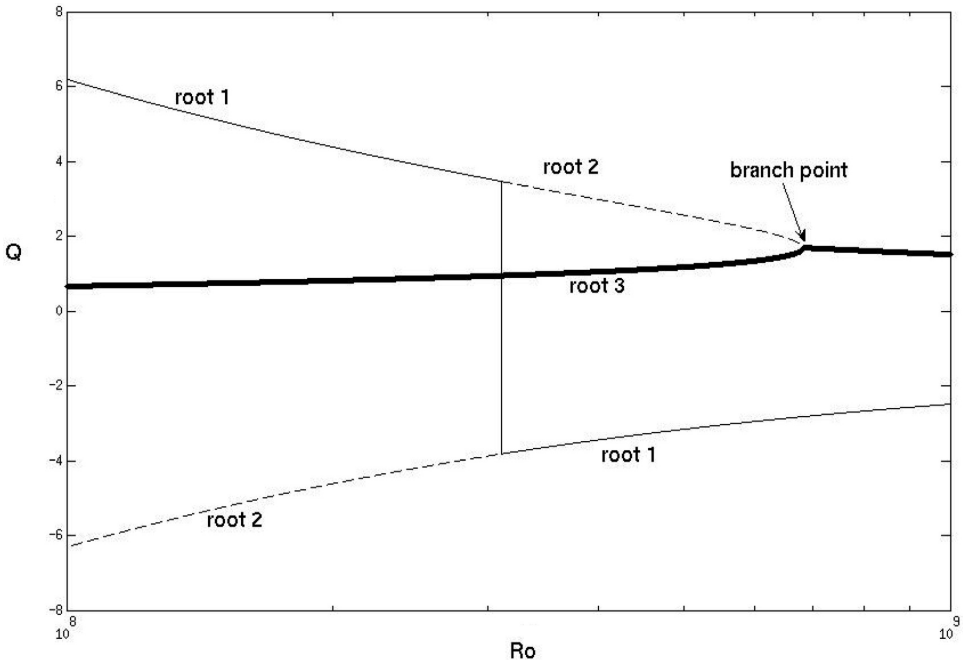

Figure A1. PBL model dimensionless variable Q vs. Rossby number Ro.

the laminar boundary layer thickness. It is a very suitable measure of how rough or smooth the PBL is at that location.

Wind profiles in the vertical are the major application here. We will use the log law or "law of the wall" valid for near neutral stability conditions:

$$u(z) = \frac{u_*}{\kappa} \log\left(\frac{z}{z_0}\right). \tag{A5}$$

Here, u_* is the friction velocity, κ is the von Karman constant $= 0.4$, and z_0 is the surface roughness height. From Eq. (A5) we find u_h, hub height velocity:

$$u_h = u_r \frac{\log(z_r/z_0)}{\log(z_h/z_0)} \tag{A6}$$

To implement our solution steps to solve for z_0, thus u_h, one would proceed as follows. We first find the single dimensionless system parameter $F = |f|(\nu/g^2)^{1/3}$. Then we select a wide range for the model independent variable Ro, say 10^8 to 10^9. Then we solve the sixth order algebraic equation (A4) for Q joining the first three branches to create a continuous solution with both a rough and a smooth branch. Then we find Re from (A3) as a function of Ro, then transform out of dimensionless space now and find u_* from the definition of Q. Finally, we get z_0 from the definition of Re and employ it in (A6) to determine u_h.

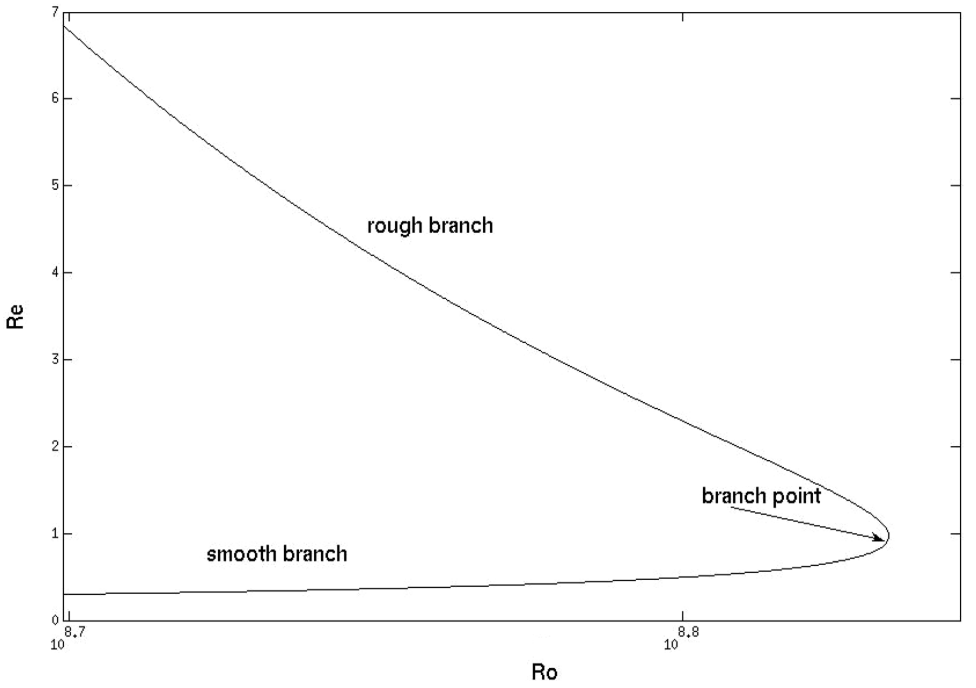

Figure A2. Reynolds number *Re* vs. Rossby number *Ro* showing both rough and smooth branches.

APPENDIX B

Impact of a vertical gradient in wind speed in the PBL wind field on available energy

The customary calculation of kinetic energy acting on a wind turbine is based on wind speed only at the turbine hub height. But the circular disk traced by the tips of a wind turbine rotor will experience differing speeds in the vertically sheared wind stream, with slower speed on the half disk below the hub and faster speed above. The log profile for $u(z)$ when cubed and integrated will produce a different kinetic energy flux than that of the customary method of calculating from the point speed at hub height z_h. In this appendix we calculate the error attendant to this customary practice.

Figure B1 presents the geometry of the disk and the wind speed profile. The differential kinetic energy flux through the elemental area ΔA is given by $\Delta P = (\rho/2)u^3\Delta A$. We take $\Delta A = w(z)\Delta z$ (see Fig. B1) with w the local breadth coincident with a chord of the circle and Δz the thickness of a differential strip of disk area. From the geometry $w = 2\sqrt{r_0^2 - Z^2}$ with r_0 the disc radius and $Z \equiv z_h - z$, that is, Z is the height relative to the hub. With the log profile for $u(z)$ from Eq. (1) we find the kinetic energy flux from

$$P = \frac{\rho}{2}\left(\frac{u_*}{\kappa}\right)^3 \int_{-r_0}^{r_0} \left[\log\left(\frac{z}{z_0}\right)\right]^3 w dZ = \rho\left(\frac{u_*}{\kappa}\right)^3 r_0^2 I$$

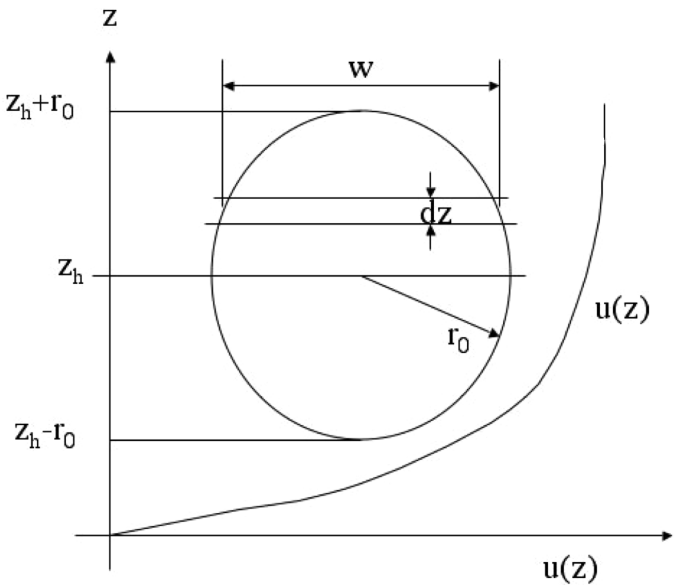

Figure B1. Schematic of the computation of net wind kinetic energy, operating on a disk of radius r_0 at hub height z_h. The rotor outline is superimposed on the curve of vertical wind shear.

where I is the dimensionless integral:

$$I = \int_{-1}^{1} \left[\log\left\{ \frac{z_h}{z_0} \left(1 + \frac{r_0}{z_h} \zeta \right) \right\} \right]^3 \sqrt{1 - \zeta^2}\, d\zeta \quad \text{and} \quad \zeta \equiv Z/r_0.$$

Note that two-dimensionless parameters emerge: z_h/z_0, which describes the character of the wind profile, and r_0/z_h, which measures the fractional extent of the disk radius relative to hub height with the range of (0,1). Larger values will cause larger deviations from vertical gradients in wind speed. In the limit of this parameter to zero, one finds that P reaches the limit for uniform speed with height:

$$P_{un} = \frac{\rho}{2} \pi r_0^2 u(z_h)^3$$

In Figure B2 we plot the ratio of these two energy fluxes vs. r_0/z_h. As expected, the ratio tends toward unity for the limit of $r_0/z_h \to 0$, i.e. as the scaled rotor radius vanishes. For example, for a rotor radius of 56 m and hub height 80 m, $r_0/z_h = 0.7$. Then for a wide range of z_h/z_0, the power ratio falls, but only to 0.98–0.99, i.e. the power falls by only 1–2%.

We conclude that the effect of finite wind shear is to reduce the turbine's actual power below that computed at hub height, but that this effect is, at most, only a few percent of reduction. This small amount we therefore ignore for the sake of simplicity. Thus the effect

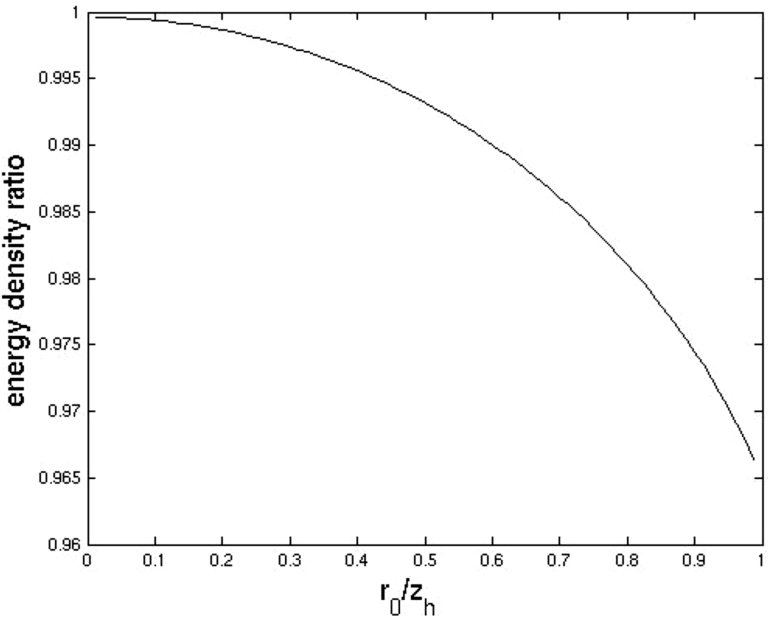

Figure B2. Ratio of wind power computed from wind speed at hub height only vs. power computed accounting for variable wind with height (vertical axis), against the ratio of disk radius r_0 to hub height z_h, (horizontal axis).

of vertical gradient is like a few other mechanisms in the model that we have omitted, including limited wind fetch and wave age.

REFERENCES

Archer, C. L. and M. Z. Jacobson. 2003. Spatial and temporal distributions of U. S. winds and wind power at 80 m derived from measurements. J. Geophys. Res., *108,* D9 4289, *doi:* 10.1029/2002JD002076.

—— 2005. Evaluation of global wind power. J. Geophys. Res., *110,* D12 110, *doi:* 10.1029/2004JD005462.

—— 2007. Supplying baseload power and reducing transmission requirements by interconnecting wind farms. J. Appl. Meteorol., *46,* 1701–1717. *doi:* 10.1175/2007JAMC1538.1

Barthelmie, R. J., M. S. Courtney, J. Hojstrup and S. E. Larson. 1996. Meteorological aspects of offshore wind energy: Observations from the Vindeby wind farm. J. Wind Eng. and Ind. Aerod., *62,* 191–211.

Barthelmie, R. J. and J. P. Palutikof. 1996. Coastal wind speed modeling for wind energy applications. J. Wind Eng. and Ind. Aerod., *62,* 213–236.

Berlinski, M. and S. Connors. 2006. Economic and Environmental Performance of Potential Northeast Offshore Wind Energy Resources, *LFEE 2006-02,* Laboratory for Energy and the Environment, Massachusetts Institute of Technology, Cambridge, Massachusetts, Jan. 2006.

Blackadar, A. K. and H. Tennekes. 1968. Asymptotic similarity in neutral barotropic planetary boundary layers. J. Atmos. Sci., *25,* 1015–1020.

Charnock, H. 1955. Wind stress on a water surface. Q. J. Roy. Meteor. Soc., *81,* 639–640.

Delaware Public Service Commission. 2007. PSC Staff Review and Recommendations on Generation Bid Proposals. Docket No. 06-241. Prepared for The Delaware Public Service Commission, May 2, 2007.

Elliott, D., C. Holliday, W. Barchet, H. Foote and W. Sandusky. 1987. Wind Energy Resource Atlas of the United States. DOE/CH 10093-4, Golden, Colorado: Solar Energy Research Institute, 210 pp.

Hess, G. D. and J. R. Garratt. 2002. Evaluating models of the neutral, barotropic planetary boundary layer using integral measures: Part I. Overview. Boundary-Layer Met., *104,* 333–358.

Kempton, W., C. L. Archer, A. Dhanju, R. W. Garvine and M. J. Jacobson. 2007. Large CO_2 reductions via offshore wind power matched to inherent storage in energy end uses. Geophys. Res. Lett., *34,* L02817. *doi:* 10.1029/2006GL028016.

Kraus, E. B. and J. A. Businger. 1994. Atmosphere-Ocean Interaction, 2nd ed., Oxford Monographs on Geology and Geophysics, no. 27, Oxford University Press, NY.

Manwell, J. F., J. G. McGowan, and A. L. Rogers. 2002. Wind Energy Explained, John Willey & Sons, West Sussex, England, 590 pp.

Monin, A. S. and A. M. Yaglom. 1966. Statistical Fluid Mechanics, Vol. 1, MIT Press, Cambridge, MA, 796 pp.

Moon, I.-J., I. Ginis and T. Hara. 2004. Effect of surface waves on Charnock coefficient under tropical cyclones. Geophys. Res. Lett., *3,* L20302, *doi:* 101029/2004GL020988

New Energy Opportunities, Inc., La Capra Associates, Inc., Merrimack Energy Group, Inc., and McCauley Lyman LLC. 2007. Assessment of Power Purchase Agreement Between Delmarva Power and Bluewater Wind Delaware LLC. Delaware Public Service Commission Docket No. 06-241, December 13, 2007.

North American Electric Reliability Council. 2005. 2000–2004 Generating availability report. Princeton, N. J. (Available at http://www.nerc.com/~gads/)

Schlabbach, J. and K.-H. Rofalski. 2008. Power System Engineering: Planning, Design and Operation of Power Systems and Equipment, Wiley-VCH Verlag GmbH & Co: Weinheim.

Turner, J. S. 1973. Buoyancy Effects in Fluids, Cambridge University Press, London, 367 pp.

Webster, P. J. and R. Lukas. 1992. TOGA COARE: The Coupled Ocean-Atmosphere Response Experiment. Bull. Am. Meteor. Soc., *73,* 1377–1416.

Wu, J. 1980. Wind-stress coefficients over sea surface near neutral conditions—a revisit. J. Phys. Oceanogr., *10,* 727–740.

Received: *9 September, 2008;* revised: *4 January, 2009.*